ORGANISATION EUROPÉENNE POUR LA RECHERCHE NUCLEAIRE
EUROPEAN ORGANIZATION FOR NUCLEAR RESEARCH
Laboratoire Européen pour la Physique des Particules
European Laboratory for Particle Physics

Occupational Health & Safety and Environmental Protection Unit

Summer Student Project Report

Response curve evaluation of the RTM661/440*lnc* RADOS device

EDMS number	prepared by	supervised by	CERN
3332357 v.1	Leonie Angerer	Helmut Vincke (HSE-RP)	CH-1211 Genève 23, Suisse
		Chris Theis (HSE-RP)	August 2025

Abstract

The RADOS RTM661/440*lnc* is a gamma counting device used for the radiological classification of materials. To characterize its response to isotropic photon-emitting sources across a range of energies FLUKA simulations are conducted. The simulated data is compared against a provided response curve and experimental measurements. A notable discrepancy is seen between the simulated response and the manufacturer's response, suggesting a need to investigate the methodology used to derive this data. Furthermore, while the simulations consistently overestimate experimental measurements, a trend is observed, where the simulated response more closely resembles the measured data as the detector size is reduced, suggesting that a precise geometric model of the device is crucial for accurate simulation. In a separate analysis, the device's six scintillation detectors are modeled individually. This confirms, that simulated values consistently exceeded measured values for all detectors, with the magnitude of the deviation varying significantly. This work serves as a starting point for validating and refining simulation models for such gamma counting devices.

Contents

1 Introduction

1.1 Classification of materials as radioactive or non-radioactive

Materials that are exposed to mixed high-energy radiation fields, such as those used at CERN facilities, are subject to activation. Due to the exposure to radiation fields the materials can potentially become radioactive. A material can be classified as radioactive in compliance with legislation if one of three criteria is met. An object is considered radioactive if

1. the dose rate at a distance of 10 cm is $\geq 100\ \frac{\text{nSv}}{\text{h}}$
2. the surface contamination is
$$\sum_{i=1}^{n} \frac{C_i}{CS_i} \geq 1 \qquad (1)$$
$C_i \ldots$ loose contamination in $\frac{\text{Bq}}{\text{cm}^2}$ of isotope i
$CS_i \ldots$ contamination limit from [1] in $\frac{\text{Bq}}{\text{cm}^2}$ of isotope i

3. the radiotoxicity S is
$$S = \sum_{i=1}^{n} \frac{\text{specAct}_i}{LL_i} \geq 1 \qquad (2)$$
$\text{specAct}_i \ldots$ specific activity ($\frac{\text{Bq}}{\text{g}}$) of the isotope i in the object
$LL_i \ldots$ legal limit (in $\frac{\text{Bq}}{\text{g}}$) from [1], defining the radioactivity of the object

The dose rate, used for the evaluation of criterion 1, can be easily measured. Criterion 2, defined by the contamination, can be dealt with by decontamination of the material. To evaluate criterion 3 on the other hand, more sophisticated methods are needed, such as gamma spectroscopy, radiochemical analysis, dedicated measurement devices such as the RADOS device and/or simulation tools to accurately determine the radiological classification of materials [2,3].

1.2 RADOS device

As briefly mentioned in the previous subchapter 1.1 the RADOS device is a measurement device meant to determine the radiological classification of potentially radioactive materials. One such device, specifically the RTM661/440*lnc* with serial number SN134 and CERN inventory number 09697, is depicted in figure 1 and is currently located at the MobiLab in front of building 892 at the CERN Prévessin cite. This gamma counting device is equipped with six plastic scintillation detectors, that are arranged in a 4π geometry. The detectors surround a measurement chamber holding a total volume of 440 l. All detectors are made of polyvinyl toluene (PVT) C_9H_{10}, are enclosed by a 3 mm aluminum housing and cover the surface area of the measurement chamber about 60%. The detectors are surrounded by a lead shielding of 3 cm thickness in the door and bottom and 5 cm in the remaining walls, to ensure low radiation background inside the measurement chamber.

The detectors at the top and bottom of the measurement chamber are type RPD25/125 detectors, while the detectors on the left, right, back and door of the chamber are type RPD40/200 detectors. The detector dimension as well as the dimensions of the measurement chamber are depicted in table 1 and were taken from [4].

Figure 1: Images of the RADOS RTM661/440*lnc* device.

Table 1: Specifications of the RADOS RTM661/440*lnc* device.

	Type	**Dimensions [cm^3]**
Measurement chamber		70 x 70 x 89.8
Detectors	RPD25/125	50 x 50 x 5
	RPD40/200	80 x 50 x 5

The RADOS device is part of the CheckPoint:Waste™ product family of *Mirion technologies* [5]. The system is a mobile, self-contained measurement station, designed to be used for clearance measurements of radioactive materials. Gamma radiation detection is conducted within the measurement chamber and the measurement results are evaluated and displayed via a connected personal computer. Each of the six large-area plastic scintillation detectors is connected to a detector module, that supplies high voltage and processes the signal. These modules are connected with the system electronics by network cables, with each module supporting two detectors. Accurate and rapid measurements are achieved by simultaneously processing multiple calculation steps. The gross count rates (direct measurement data in counts per second) from the detectors are corrected for background radiation and converted to mass-specific activity using calibration factors. These factors depend on user-defined and system-internal parameters. The filling level, indicating up to which height the object fills the container, must be specified by the user as one of the following options and individual calibration has to be performed.

- 1% to 25%
- 25% to 50%
- 50% to 75%
- 75% to 100%

The user also defines the relative radionuclide inventory, that is normalized to 100% and allows for automatic calculation of the exemption limit and the activity fractions of each radionuclide. Furthermore, the disposal path must be selected, as it determines the applicable clearance levels or safety factors. Additionally, the material type of the object must be defined, allowing the system to apply an appropriate surface-to-mass ratio for surface contamination calculations and subtract any natural activity from the final results. Some parameters are determined by or already stored in the device. This includes the background radiation count rate, which accounts for ambient radiation and electronic noise. The object's weight is measured by an internal scale with a precision of 0.1 kg. The system also accounts for background reduction, defined as the difference between the background signal with the chamber empty and with the object inside. This reduction is attributed to both the additional shielding provided by the object and the decrease in air volume within the measurement chamber due to the object [4,6].

1.3 Count rate of the RADOS device

The count rate response of the RADOS device to a sample of homogeneously distributed radioisotopes, can be calculated with the help of the response function using the following equation 3 [3].

$$\text{Count rate} = \sum_{i=1}^{n} \sum_{j=1}^{k} \text{RF}(E_{i,j}) \cdot I_{i,j} \cdot \text{specAct}_i \cdot m \tag{3}$$

m ... sample mass
specAct_i ... activity per gram of the isotope i
$I_{i,j}$ ... intensity of the given photon j per decay of the isotope i
$\text{RF}(E_{i,j})$ ... RADOS response to a photon with an energy of $E_{i,j}$
$E_{i,j}$ ... energy of the photon j emitted from the isotope i

Arbitrary samples consist of a mixture of nuclides, that are uniformly distributed throughout the sample's volume. Every radionuclide has a specific activity, denoted as specAct_i and emits a characteristic photon spectrum upon decay, that is quantified by the photon emission intensity $I_{i,j}$. To calculate the total count rate, the RADOS responses to all individual photons emitted by the sample must be summed, accounting for the different isotopes and their respective emission probabilities. Since radioactivity is given as specific activity (Bq/g), the total detector count rate must also include the sample's mass [3].

1.4 Leading nuclide correlation (lnc) method

RADOS RTM*lnc* devices are calibrated using artificial ^{60}Co sources. These sources provide calibration factors for converting the measured net count rates into ^{60}Co equivalent activities. The calibration factors vary depending on measurement conditions, such as object geometry, container filling level and sample mass. To estimate the activity of radionuclides other than ^{60}Co, RADOS developed the Leading Nuclide Correlation (lnc) method. As depicted in equation 4, the lnc factor for a radionuclide b, denoted as lnc_b, translates the detector's response M in terms of ^{60}Co equivalent activity (net machine counts per second converted to ^{60}Co equivalent activity) into the activity of the specific radionuclide A_b [6].

$$A_b = \frac{M}{lnc_b} \tag{4}$$

A_b ... activity of radionuclide b $[\mathrm{Bq}_b]$
M ... measurement result $[\mathrm{Bq}_{^{60}\mathrm{Co}}]$
lnc_b ... correlation factor for radionuclide b $\left[\frac{\mathrm{Bq}_{^{60}\mathrm{Co}}}{\mathrm{Bq}_b}\right]$

The lnc method assigns fractions of the total measured gamma signal to the individual radionuclides, based on their gamma emission profiles and their relative activity in the radionuclide inventory, that is defined by the user. RADOS supplies a set of lnc factors for the most commonly encountered radionuclides. These lnc factors are determined for a representative average of volume-to-mass ratios. In order to account for variability across different object geometries and material densities, an additional safety factor is applied. For radionuclides that emit no significant gamma radiation, the corresponding lnc factor is set to zero. In such cases, the activity of these radionuclides must be estimated through calculations and added separately to the overall measured activity [6].

2 Simulations

To simulate the functionality of the device described in the previous subchapter 1.2, the Monte Carlo simulation code FLUKA version 4.5 [7] is used. This code was developed and is maintained by CERN and is designed to model the interaction and transport of particles through matter with high precision. It uses probabilistic Monte Carlo methods to simulate individual particle trajectories and stochastic interactions based on known physical cross sections and decay probabilities. This allows it to predict how radiation behaves in complex geometries and materials, including secondary particle production, energy deposition, and shielding effectiveness. FLUKA supports a wide range of particles and energies, making it particularly suitable for accelerator design and radiation protection studies [7].

The goal is to simulate the response of the RADOS device to an isotropic, photon emitting point source as well as several volume sources of different mass, that are placed in the center of the measurement chamber. The geometry of the RADOS device was constructed according to the previously mentioned specifications in subchapter 1.2 using the software SimpleGeo version 4.3 [8] from which the geometry is exported and loaded into a FLUKA input file.

In figure 2 the constructed geometry is depicted. It should be mentioned that for the geometry of the device only the parts up until the lead shielding of the device were taken into account, as this is the relevant part for the simulation and no photon reaching the area beyond the lead shielding will contribute to the count rate detected by the RADOS device.

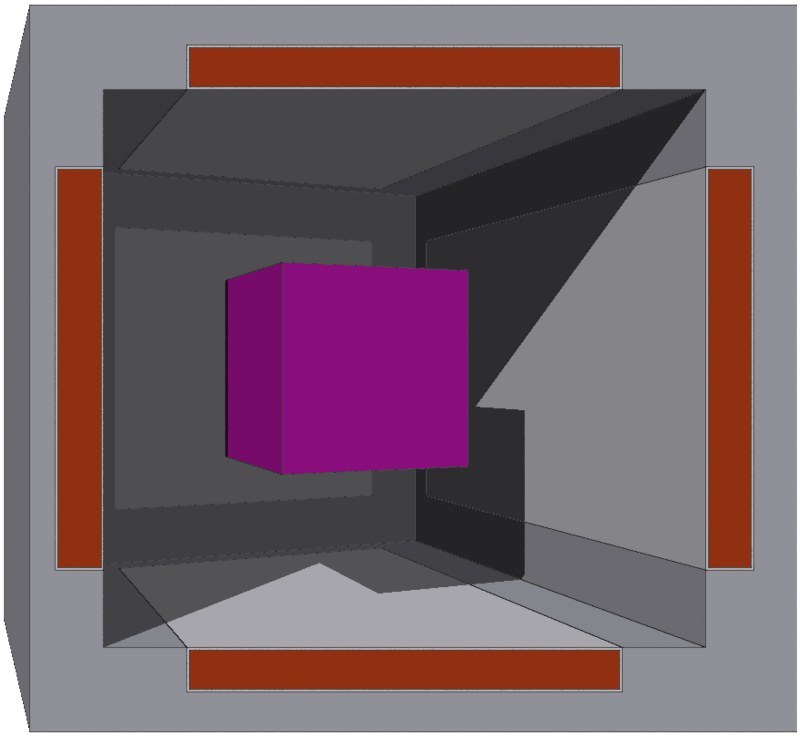

Figure 2: Constructed geometry of the RADOS device. Purple = volume source, brown = scintillation detectors, light grey = aluminum housing of the detectors, dark grey = lead shielding.

In order to obtain the response of the RADOS device to an isotropic source with arbitrary photon spectrum, the response of the detector to monoenergetic photons emitted from the source is calculated for an energy range of 50 keV to 10 MeV. For every given energy, the monoenergetic photons are emitted isotropically from the point source or isotropically and uniformly from within the cubic volume source. To simulate arbitrary volume sources that are comparable to real life materials needing to be classified, the material that is used has the same chemical composition of iron (Z=26, A=56) but an apparent density of 2.5 $\frac{g}{cm^3}$. To simulate materials of the same composition but different mass, the size of the cubic sources is varied according to table 2.

Table 2: Specifications of the cubic volume sources used in the simulation.

Mass [kg]	1	2	5	10	20	50
Edge length [cm]	7.4	9.3	12.6	15.9	20	27.1

During the simulation, some of the emitted photons reach one of the six scintillation detectors and make an energy deposition inside it, that is registered for each single emitted primary photon using FLUKA DETECT cards. These DETECT cards simulate a physical detector by counting energy depositions as discrete values in a histogram. A region is specified in which the energy depositions are counted within a defined energy range on an event-by-event basis. In this case the six scintillator detectors of the RADOS device are unified in one detector region in which the energy depositions are counted. The energy range is evenly divided into 2000 channels, so that a recorded energy deposition is counted in the channel corresponding to the energy of the deposition, similar to the behavior of a real analog-to-digital (AD) converter. It should be mentioned that the FLUKA DETECT card can only be run in analog mode since biasing can influence the results [7]. Furthermore, in order to not exclude any physical processes the electron-positron kinetic energy transport threshold is set to 10 keV. The minimal energy that is to be detected as an energy deposition is set to 50 keV. Energy depositions below this threshold cannot be reliably attributed to detected photons rather than noise. These values are therefore excluded from the analysis.

3 Simulation results

3.1 Fluence results

The fluence is simulated in FLUKA using a USRBIN card [7]. Figure 3 depicts the spatial distribution of the photon fluence of an isotropic point source emitting photons with an energy of 80 keV. The grey area in this figure 3 corresponds to the lead shielding, that is part of the RADOS geometry (see figure 2). The shielding is surrounded by a vacuum depicted in white and a void shown in black, that were introduced for the sake of the simulation. The image is a side view of the geometry of the RADOS device, therefore the shielding is less thick on the right side of the image, where the door of the measurement chamber is located. This in accordance with the dimensions specified in subchapter 1.2.

The photon fluence denotes the number of photons passing through a unit area. It reaches its maximum near the center of the detector, where the primary photons are emitted from the point source. As the photons propagate isotropically away from the point source, the fluence decreases with distance due to geometric spreading. As can be seen from the fluence values at the outer edges of the detector, some photons reach the surrounding shielding. Since the simulation only includes the point source without any additional shielding, the resulting photon fluence distribution remains largely unchanged when the photon energy is increased. However, a slight difference can be observed, at higher photon energies, a greater number of photons reach the surrounding shielding.

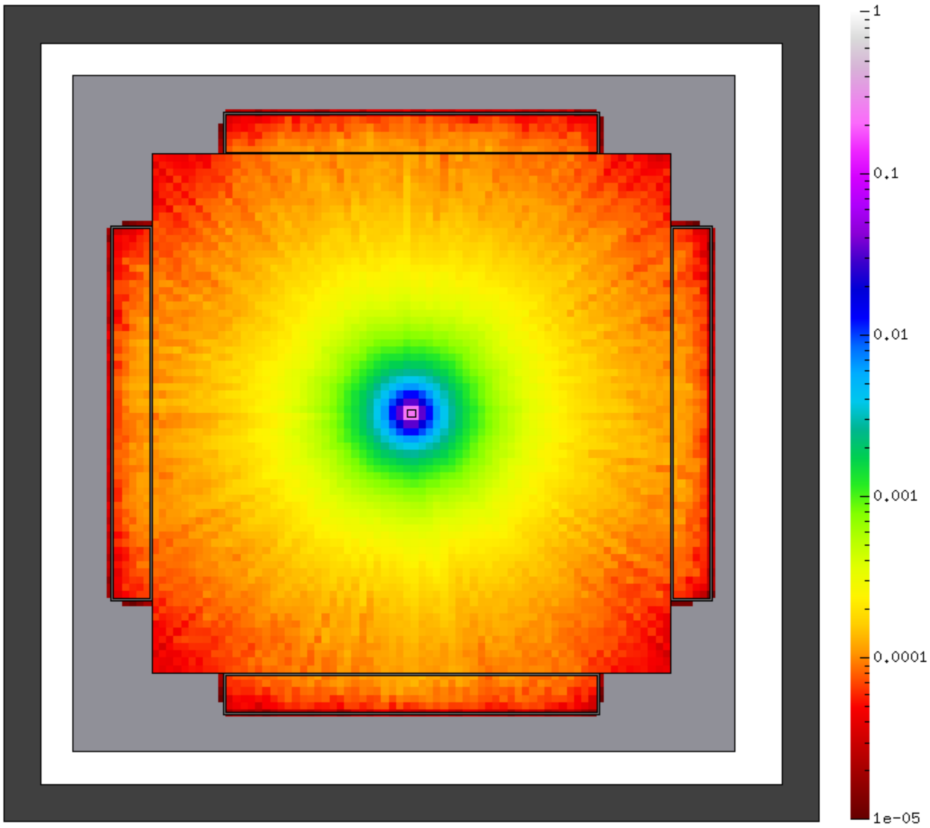

Figure 3: Photon fluence in the RADOS device per primary photon of 80 keV energy, started from an isotropic point source. (grey = lead shielding, white = vacuum, black = void).

Figure 4 depicts the photon fluence of a 50 kg volume source for the energies of 80 keV and 1 MeV. When examining the volume source in figure 4a, corresponding to a photon energy of 80 keV, one can see that the photons are uniformly started from within the volume source and emitted isotropically from it. Due to the relatively low photon energy not many photons reach the detectors in this case. However in figure 4b, corresponding to a photon energy of 1 MeV, many more photons reach the detectors and some even reach the shielding.

It should be noted that the color scale used in the fluence results for the 50 kg source of figure 4 has been adjusted compared to the result for the point source in figure 3. When comparing the fluence distributions of the two sources for a photon energy of 80 keV, it becomes clear that the volume source results exhibits significantly lower overall fluence values and a smaller travel distance of the photons. This reduction is due to the uniform distribution of the primary photons within the volume source and the interaction of the photons with the source material, that limits the distance photons can travel. For the point source photons can travel further because they are not shielded by any (source) material.

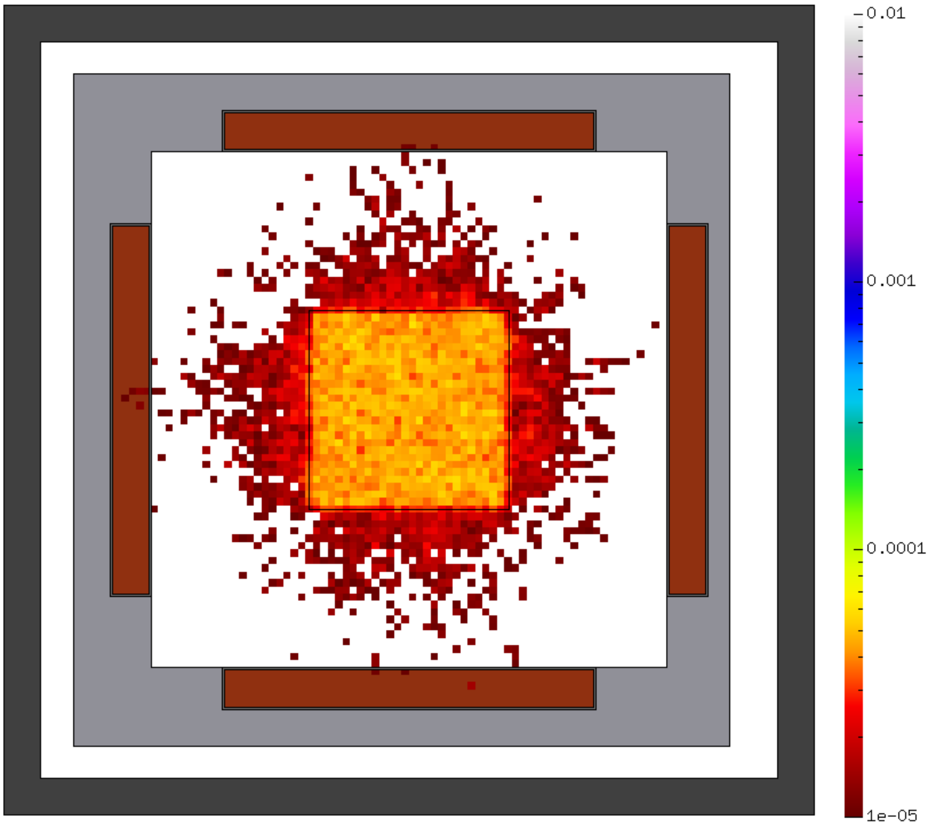

(a) 80 keV photon energy.

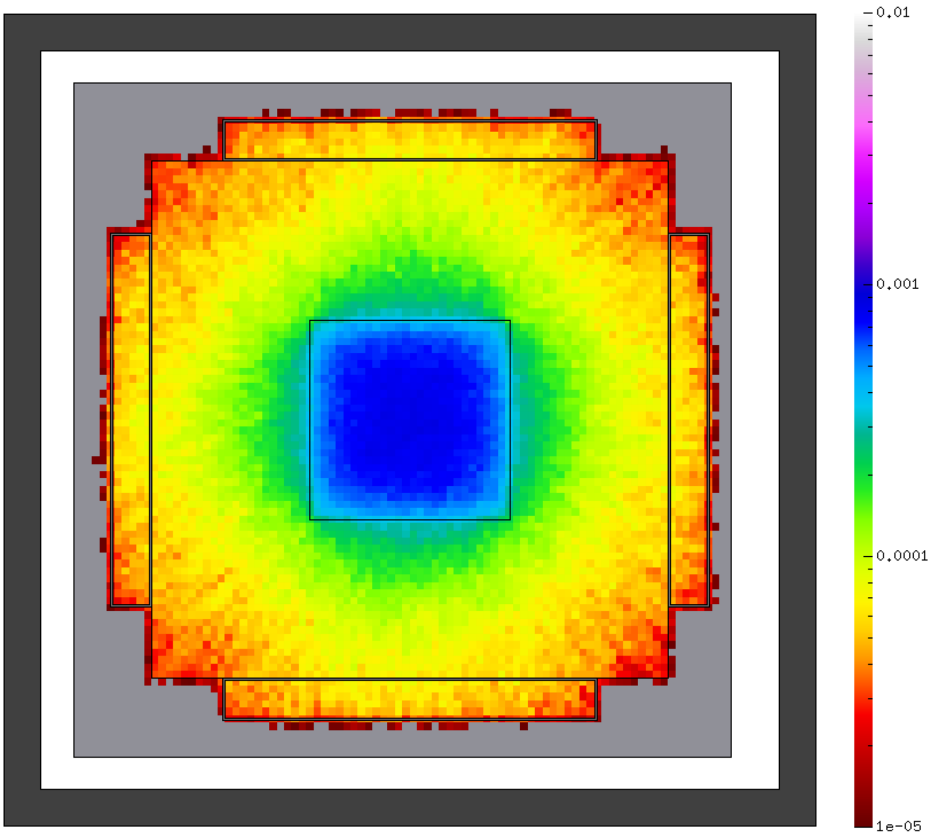

(b) 1 MeV photon energy.

Figure 4: Photon fluence in the RADOS device per primary photon, started from an isotropic 50 kg volume source.

3.2 Energy deposition in the detector

In figure 5 the energy deposition spectrum in the RADOS detector region, when simulating an isotropic point source of 1333 keV is depicted.

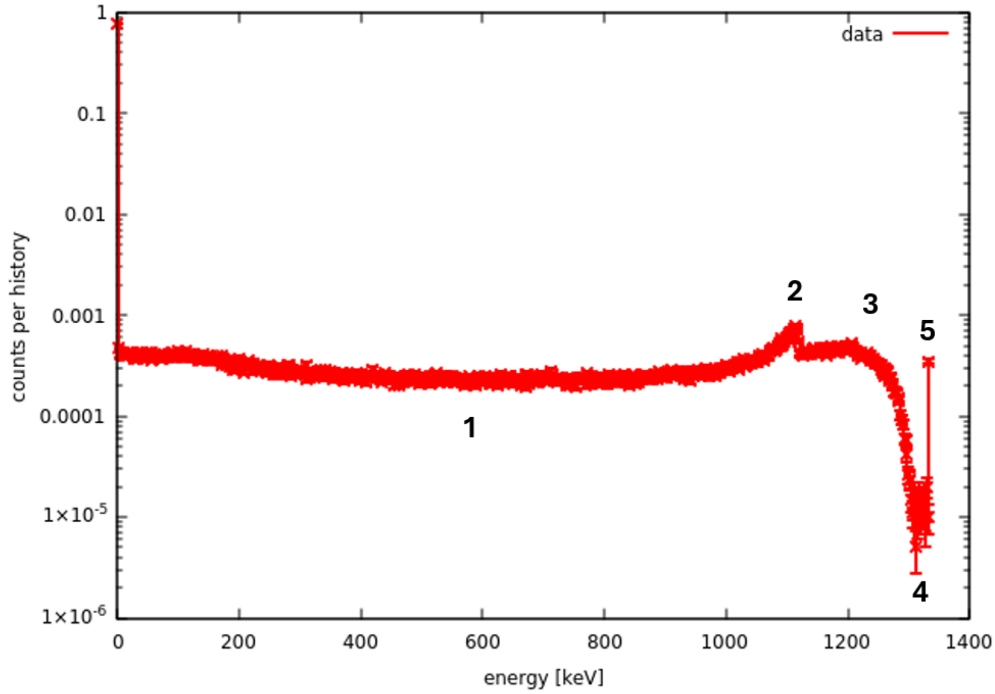

Figure 5: Energy deposition spectrum in the RADOS detector region from a isotropic point source emitting photons with an energy of 1333 keV.

The maximal energy deposition in this plot is given by the energy of the emitted primary photons of 1333 keV. In all cases involving lower energy depositions within the detector, the incoming photons interact with the material of the scintillation detectors (or their aluminum housing) and loose some of their energy through the escape of secondary particles. At an energy of 0 keV in the plot all events with 0 keV energy deposition are counted, therefore the value for the counts per history is close to one in this case.

A significant part of the recorded spectrum can be attributed to Compton Scattering. During this process photons scatter at different scattering angles, leading to a range of deposited energies. This can be described by the following equation 5 [9].

$$E_{\gamma'} = \frac{E_\gamma}{1 + \frac{E_\gamma}{m_e \cdot c^2} \cdot (1 - \cos(\theta))} \tag{5}$$

$E_{\gamma'}$ ... energy of the scattered photon
E_γ ... energy of the initial photon
$m_e \cdot c^2$ = 511 keV ... rest energy of the electron
θ ... scattering angle between 0° to 180°

The maximum energy deposition for Compton scattering is reached at a scattering angle of 180°, where the scattered photon has an energy of $E_{\gamma'} \approx 214$ keV and the transferred energy is therefore $E_{\gamma} - E_{\gamma'} \approx 1119$ keV. At this energy the Compton edge is visible in figure 5 and is labeled with the number 2. The hypothetical limit on the lower energy range of Compton scattering is reached at an scattering angle of 0°, where no energy is deposited. The Compton range therefore covers the range of 0 to 1119 keV and is denoted as the number 1 in figure 5.

The peak at 1333 keV corresponds to the photopeak and is labeled as the number 5 in figure 5. In this event the entire photon energy is deposited in the detector, in most cases via the photoelectric effect. The peaks slightly below the photopeak, denoted as the number 4, are photoescape peaks. An X-Ray is produced via the photoelectric effect and escapes, while the remaining energy of the primary photon is absorbed. The range between the Compton edge and the photoescape peaks, that is labeled with the number 3, can be attributed to events involving multiple scattering processes. Due to the combination of the low Z of the detector material and the photon energy just above the pair production threshold (1.022 MeV), peaks at energies of 511 keV as well as the single (E - 511 keV) and double (E - 1.022 MeV) escape peaks are overshadowed by the Compton range of the spectrum.

3.3 Detector response

To evaluate the response of the RADOS device to monoenergetic photons, a series of Monte Carlo simulations are conducted using FLUKA. In these simulations, photons of discrete energies are used, that are emitted isotropically from a point source. An event is detected when the energy deposited within the detector region exceeds a threshold of 50 keV. This threshold accounts for the minimum deposited energy required to produce a measurable signal in the detector, that can be clearly distinguished from noise. (It should be mentioned, that this value is estimated and should be evaluated more closely by a dedicated analysis of the detector output signal.) For each incident photon energy, the RADOS response is defined by the number of detection events per emitted photon and can be interpreted as the average probability for a photon to be detected by the detector through an energy deposition above 50 keV. This simulation is repeated for 35 photon energies ranging from 50 keV to 10 MeV to get a grasp of the sensitivity and efficiency of the simulated RADOS device as a function of photon energy for the given sample material and geometry. This simulation is repeated for volume sources with varying masses of 1, 2, 5, 10, 20, and 50 kg. The sources are simulated as cubes made of iron with an adapted, apparent density of 2.5 $\frac{\text{g}}{\text{cm}^3}$. To achieve the desired masses, the edge lengths of the cubes are varied as specified in table 2. In these simulations, the photons of a given energy are uniformly distributed throughout the respective volume source and emitted isotropically from it. The response for each energy point was calculated by simulating 10^6 primary photons histories. The resulting response data is depicted in figure 6 with the respective uncertainty obtained from the simulation. A cubic spline interpolation is applied to model the behavior of the data. The complete set of response values is provided in appendix A.

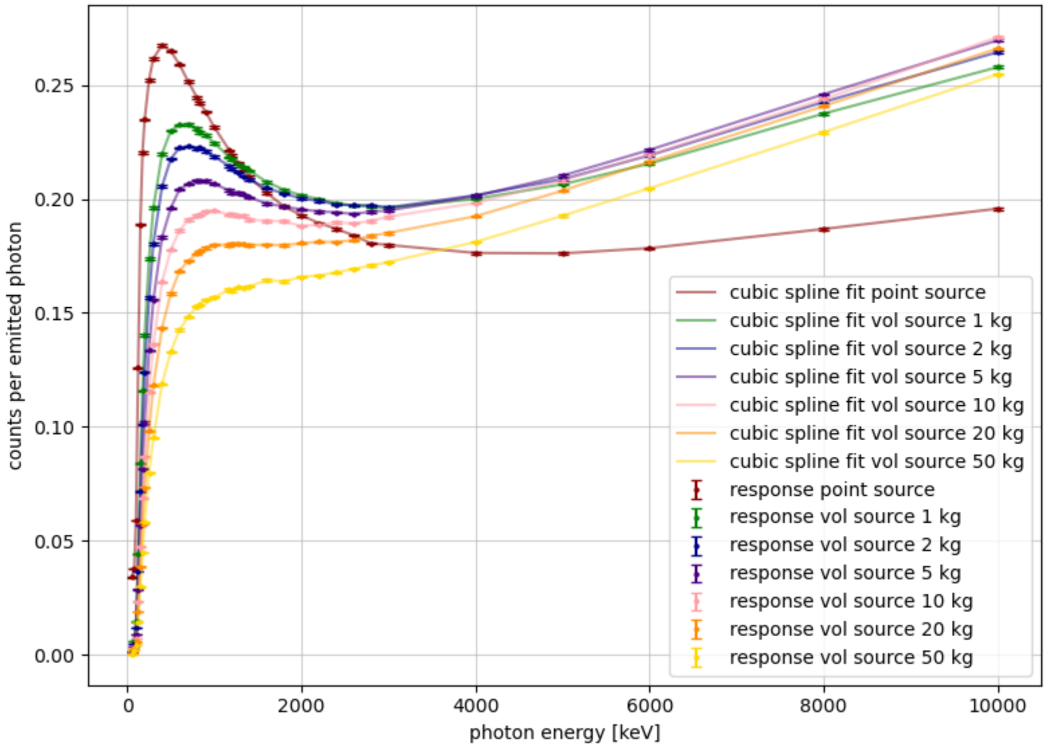

Figure 6: Simulated response curve of the RADOS device for isotropic sources emitting with an energy in the range of 50 keV to 10 MeV from either a point source or from volumetric sources of varying masses. The response indicates the probability for a single photon emitted at a given energy to be registered.

All response curves in figure 6 show low response values at low photon energies. Photons with low energy are prone to be absorbed in the aluminum housing of the detectors, which decreases the number of detected photons significantly. Furthermore, when photons with energy close to the minimal energy threshold of 50 keV reach the detector, they would need to deposit the majority of their energy in the detector region in order to be detected. Because only a small number of photons achieve such a deposition, the number of detected photons is low. With increasing photon energy, the probability for the photons to traverse the aluminum housing and make an energy deposition above 50 keV in the detector region increases significantly resulting in a steep increase in response with photon energy, that is evident in figure 6. Around 400 keV each curve exhibits a distinct peak in response, followed by a slight decrease and then a gradual increase with higher photon energy. For the point source, this 400 keV peak represents the global maximum, whereas the volume sources continue to increase, reaching their respective global maxima at the highest simulated energy of 10 MeV. At the 400 keV peak, the lighter volume sources show a slightly higher response than the heavier ones. At higher photon energies, the point source yields a significantly lower response than the volume sources. Among the volume sources, the response curves closely resemble each other in this high-energy range, with the 50 kg source consistently showing a slightly lower response than the others. The trend, that the response of the volume sources increase significantly more than that of the point source at high photon energies, can be attributed to the interaction of the primary photons with the source material. Through interaction (eg. electron - positron pair formation) more photons are produced, which increases the probability to detect one of these photons.

A comparison between the simulated response data shown in figure 6 and a reference response provided by *Mirion Technologies* [5], the manufacturer of the RADOS device, is made. Because the manufacturer's response data is confidential, it cannot be provided in this report, however a detailed comparative description is included. Since the manufacturer's data is normalized to the response for ^{60}Co and limited to photon energies up to 3 MeV, the simulated response curves are handled in the same way to allow for direct comparison. ^{60}Co emits two gamma rays at the energies of 1.173 MeV and 1.332 MeV, both of which in about 99% of decays. To normalize the simulated data accordingly, a normalization factor is calculated by summing the the response at 1.173 MeV using a weight of 0.9985 and the response at 1.332 MeV weighted with 0.999826. All simulated response values are then divided by this normalization factor. Upon comparison, the simulated data align well with the manufacturer's data at the energies of 1.173 MeV and 1.332 MeV, that correspond to the gamma emission lines of ^{60}Co. However, at lower photon energies, the simulated data consistently shows a higher response. Out of the simulated cases, the 50 kg volume source yields a response most similar to the manufacturer's data in this lower-energy range. At higher photon energies the volume source response data exceeds the manufacturer's response, with the 1 kg volume source being the best match. The only case where the simulated response remains below the manufacturer's data is the point source at higher photon energies. It is evident that the simulated response data exhibits a noticeable deviation to the provided data.

An additional simulation is conducted to try and minimize the deviation. Since the simulation of the 50 kg volume source yields the most similar response compared to the manufacturer's data, the new simulation involves a simulation of the 50 kg volume source placed at the bottom of the measurement chamber. Since the RADOS device is equipped with a scale at its base and requires a minimum mass to register a measurement, it seems that the system is designed for this source placement. This simulation aims to assess whether and how the change in position of the source influences the response results. In this simulation the 50 kg volume source is defined as a cube with an edge length of 27.1 cm, as defined in table 2 and consists of the same material as the previously simulated volume sources, namely iron with an adapted, apparent density of 2.5 $\frac{g}{cm^3}$. Instead of placing this source in the center of the measurement chamber like in the previous simulation (placement can be seen in figure 2 of the geometry), the source is placed on the bottom of the measurement chamber in the middle of the bottom detector. The simulation procedure is precisely the same as for the previous simulations.

In figure 7 a comparison between the response curves of the previous simulations and that of the 50 kg volume source placed at the new position is depicted. Both placement variants of the 50 kg source exhibit similar overall shapes. However, the source positioned at the bottom of the measurement chamber (brown) consistently yields higher response values than the one placed in the center (yellow), particularly at higher photon energies, where it shows the maximum overall response. This is likely due to the photons having a longer travel path through the bottom detector, which increases the probability of detection.

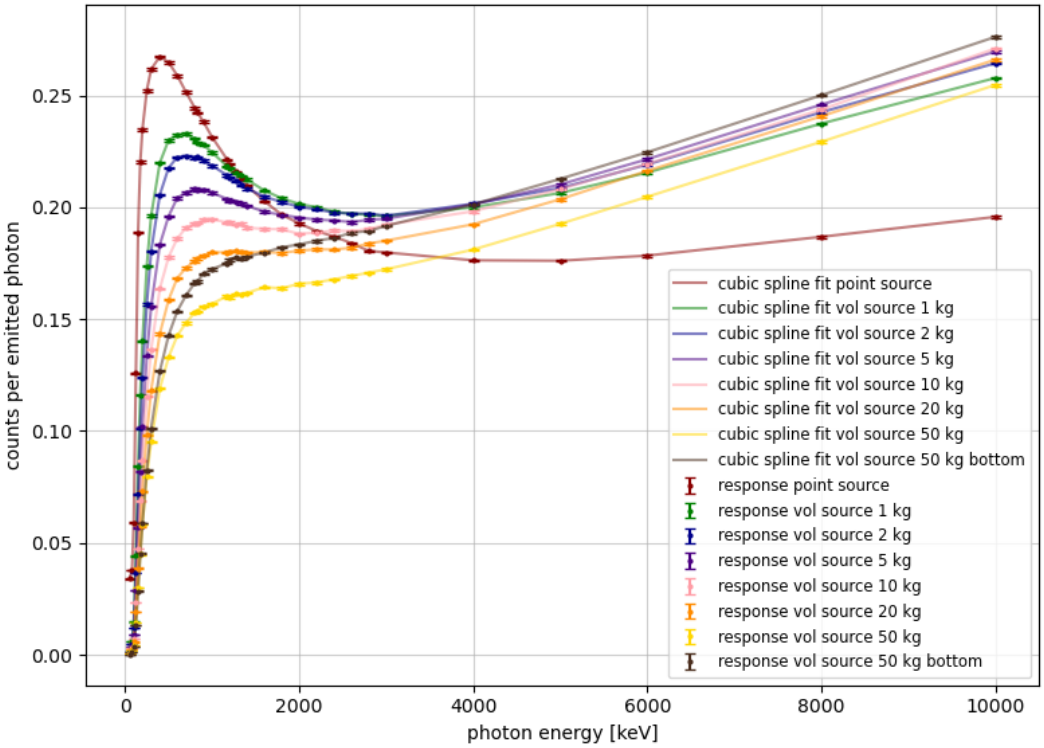

Figure 7: Simulated response curve of the RADOS device for isotropic sources emitting with an energy in the range of 50 keV to 10 MeV, including the 50 kg volume source placed on the bottom of the measurement chamber (brown).

Table 3 depicts a comparison between the response values of the simulations of the point source and the 50 kg source with different placements. The response per photon values for the simulations are obtained through a calculation of the count rate with equation 3, using the response values from from the cubic spline fit at the energies of the respective gamma emission lines of ^{60}Co and ^{137}Cs and the activities and intensities of the sources, depicted in table 4. The obtained count rate in cps is then expressed in terms of photons per second using the values of table 4. The uncertainty of the response values can be assumed to be in the order of the uncertainty of the simulation, namely 0.2%. Both simulations for the 50 kg source with different placements show a lower response at these energies than the point source. This can be attributed to the self-shielding properties of the volume sources.

Table 3: Simulated response per emitted photon for an isotropic point source and a 50 kg volume source placed in different positions.

Nuclide	E_γ **[keV]**	**Response per** γ **[$\frac{\text{cps}}{\gamma/\text{s}}$]**		
		point source	50 kg source (center)	50 kg source (bottom)
^{60}Co	1173, 1332	0.2170	0.1606	0.1759
^{137}Cs	662	0.2544	0.1463	0.1582

A comparison between the normalized response values from the simulation and the reference data provided by the RADOS device manufacturer is made. At low photon energies, the response of the newly positioned 50 kg source aligns slightly more closely with the manufacturer's curve than the previous placement. In contrast, at higher photon energies, the simulated response exceeds the manufacturer's values significantly and shows a greater deviation than the 50 kg with the initial placement.

The origin of the deviation between the simulated data and response curve provided by the manufacturer is currently not fully understood. The methodology used to generate the manufacturer's data is not disclosed in detail but it is presumed to involve a combination of measurement data and simulation. It is likely that the manufacturer's curve was designed to be conservative, which may account for the observed differences.

4 Measurement

The measurements outlined in this chapter were performed using the RADOS RTM661/440*lnc* device described in subchapter 1.2. As a first step, the device has to measure the background in the empty measurement chamber for a set amount of time. After the background measurement is completed it is valid for a period of an hour until the next background measurement has to be carried out. The background measurement starts automatically when the measurement chamber is empty and the door is closed. Before performing a measurement with the RADOS device, a constancy check has to be carried out. This check must be performed at least once daily before conducting measurements, however, more frequent checks are recommended to ensure optimal performance of the device. To perform the constancy check a ^{60}Co source with ID number 3718 (Activity 10.11 kBq as of 12.11.2024) is used, that is stored in a respective container next to the detector and secured with a combination lock. The source is placed in the center of the measurement chamber with the help of a platform attached to a chain, that is hung from the top of the device. To pass the constancy check the respective counts in the six scintillation detectors cannot deviate from each other more than a given count interval for a period of 120 s. (For more detailed information on this step see [10].) After the constancy check is passed, measurements are carried out using two sources with parameters as depicted in table 4.

Table 4: Source parameters and emission characteristics of ^{60}Co and ^{137}Cs. (Activity as of 23.07.2025).

Nuclide	Source ID	Activity [kBq]	Intensity	Photons/s
^{60}Co	4999.1	18.018	2	36036
^{137}Cs	4999.8	35.28	0.85	29988

The values for the photons, that are emitted by the respective nuclei per second, can be described by the product of the activity and the respective intensity. The intensity can be understood in the sense that ^{60}Co emits two photons with energies 1.173 MeV and 1.332 MeV per decay in nearly 100% of cases. ^{137}Cs however, emits a photon with an energy of 662 keV in 85% of decays.

To perform the measurement, the material placed inside the RADOS device, has to exceed a minimal equipment mass, specific to the type of material. Because the two sources in table 4 do not fulfill this condition, a brick of 11.2 kg is placed on the bottom of the measurement chamber, as the RADOS device is equipped with a scale in the lower part of the geometry. Some additional parameters need to be specified, such as the type of material as in this case metal (other classifications include electronics, cables, concrete, burnable) and the filling level of 1% to 25%. The radionuclide vector is specified as ^{60}Co only. (For more detailed information on the operation of the RADOS device see [11].) Since only the pure count rate (no interpretation towards specific activity of the sample) is extracted from the measurement, the provided parameters do not influence the measurement result. Two measurements of 120 s each were carried out using the sources specified in table 4 yielding the results depicted in table 5. The uncertainty of the measurement values can be considered to be under 1%.

Table 5: Response of the RADOS RTM661/440*lnc* to ^{60}Co and ^{137}Cs.

Nuclide	Response [cps]	Measurement time [s]
^{60}Co	6370	120
^{137}Cs	5530	120

5 Comparison of simulation and measurement

To be able to compare the measured data to the simulations, the response values of table 5 are represented in terms of photons emitted per second of table 4, to obtain the response per emitted photon. For the simulation of the point source the response per emitted photon is obtained from a count rate calculation with equation 3 using the response data from the cubic spline fit for the respective photon energies, depicted in table 6. The uncertainty of the response values can be assumed to be in the order of the uncertainty of the simulation, namely 0.2%.

Table 6: Comparison of the measured data to the simulated data for an isotropic point source.

	Measurement		Simulation	
Nuclide	Response [cps]	Response per γ [$\frac{\text{cps}}{\gamma/s}$]	E_γ [keV]	Response per γ [$\frac{\text{cps}}{\gamma/s}$]
^{60}Co	6370	0.1767	1173, 1332	0.2170
^{137}Cs	5530	0.1844	662	0.2544

As seen in table 6 the measured response deviates from the simulated response. To characterize this deviation, the Measurement-to-Simulation Ratio (MSR) is introduced, defined as the ratio of detected photons by the measurement versus the simulation. This ratio is depicted in table 7 and can be interpreted in the sense that for the case of ^{60}Co, approximately 81% of the photons predicted by the simulation with the point source to be detected, were actually detected in the measurement. Furthermore, the measured lnc factors are depicted in table 7. The uncertainty of the MSR and lnc values can be assumed to be under 1%, taking into account the uncertainties of the simulation and measurement.

Table 7: Average measured lnc factors per photon and ratio of the measured response of the RADOS RTM661/440*lnc* relative to the simulated response (MSR).

Nuclide	lnc per γ	E_γ [keV]	MSR
^{60}Co	0.5	1173, 1332	0.81
^{137}Cs	0.498	662	0.73

The origin of this deviation is currently not fully understood. However, several strategies have been proposed to investigate its cause. One approach is to perform a simulation in which each of the six detectors is defined as a separate region. In practical measurements using the RADOS device, data from all six detectors are recorded individually and then summed. Comparing such simulation results with measurement data may help determine whether the deviation originates from a particular detector or whether all detectors exhibit slight differences.

A second strategy is to perform a simulation using a slightly thinner detector geometry. According to subchapter 1.2, the detector thickness is specified as 5 cm, which was obtained from the RADOS manual [4]. However, the manual does not clearly state whether this includes the aluminum housing. Previous simulations assumed a 5 cm thickness excluding the housing. Running a simulation that includes the aluminum housing within the 5 cm specification may yield results more consistent with the measurements.

5.1 Additional simulations

This subchapter provides the results of the two strategies to uncover the cause of the deviation between the measured response data and the simulated data, that were proposed at the beginning of chapter 5.

5.1.1 Separating the detector regions

A simulation is conducted in the same manner as described in chapter 2 with the change that the six scintillation detectors of the RADOS device, that are the top, bottom, left, right, rear and front detector, are defined as separate detector regions. All recorded counts of a detector are counted in the respective region. Figure 8 depicts the resulting response curves for the separate detector regions. It is evident that the response of the top and bottom detectors are significantly smaller than that of the other detectors. This can be attributed to the smaller size of these two detectors, that is specified in table 1, and the different distances between source and detectors.

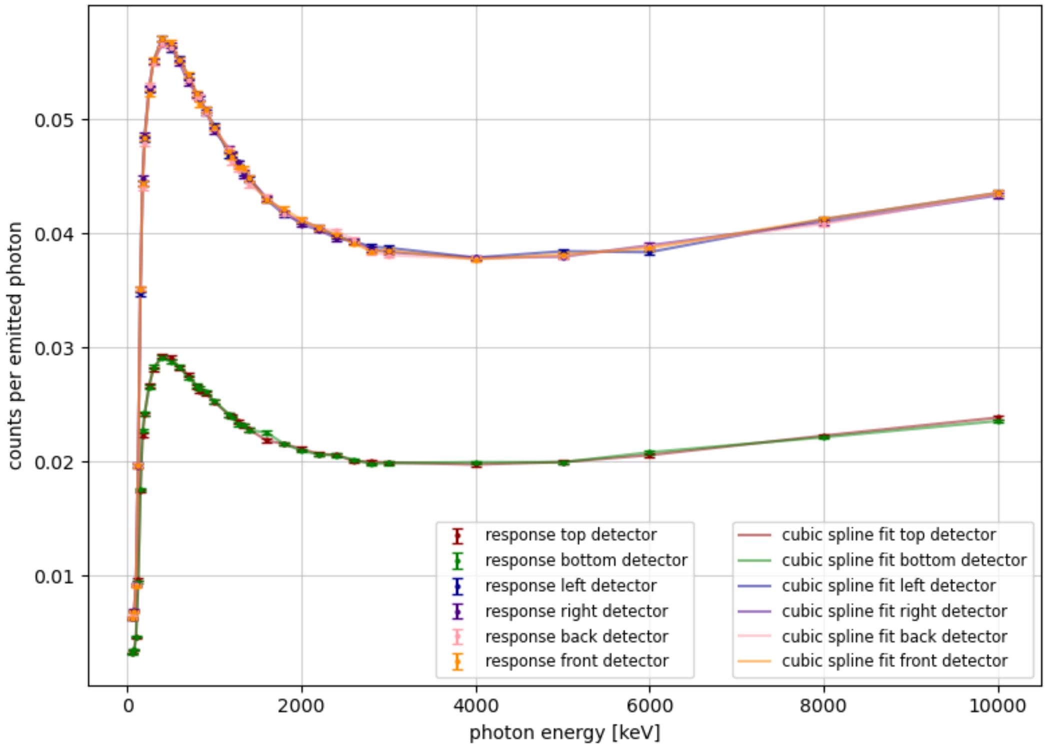

Figure 8: Simulated response curve of the six scintillation detectors of the RADOS device simulated as separate detector regions. The source is an isotropic point source emitting with an energy in the range of 50 keV to 10 MeV.

To compare the simulation with measurement data, the measurements of the ^{60}Co and ^{137}Cs sources placed at the center of the measurement chamber are used, which are depicted in table 6. The RADOS device provides response data for each detector separately, as well as the sum of the detector counts. Tables 8 and 9 present the responses from both measurements and the response calculated from the simulation values for the individual detector regions of ^{60}Co and ^{137}Cs respectively. Additionally, the Measurement-to-Simulation Ratio (MSR) is provided.

Considering the uncertainties of both the simulations, that are in the range of 0.5 to 0.7%, and the measurements, that can be considered to be lower than 1%, the uncertainty of the MSR can be regarded as being below 1% also. For the ^{60}Co source, all detectors show MSRs ranging from 69% to 79%, with the bottom detector displaying the lowest value and the right detector showing the highest value. The top, left and front detector all show an MSR of 76% and the rear detector shows a slight deviation with 77%. In the case of the ^{137}Cs source, all detectors exhibit ratios between 61% and 74%, with again, the bottom detector showing the lowest value and the right detector exhibiting the highest value. Overall the top, bottom, and left detectors show lower values compared to the others.

In general, the measured response is lower than the simulated response for all individual detectors in both cases. The simulation assumes symmetry between opposing detectors (top and bottom, left and right, rear and front), which is reflected in the very similar response values for each case, shown in tables 8 and 9. However, the measurement values reveal greater deviations between opposing detectors compared to the simulation. Moreover, no consistent trend of deviation for specific detectors is observed, except that the bottom detector exhibited the lowest overall

MSR and the right detector showed the highest overall MSR in both cases, although the magnitude of deviation varied between measurements. This variability is likely due to slight differences in the sensitivity or read-out efficiency of the detectors. In order to understand the behavior of the individual detectors of the RADOS device better, further simulations and measurements would need to be conducted with different energies and different placements of the source.

Table 8: Ratios of the measured response of the RADOS RTM661/440*lnc* relative to the simulated response (MSR) for the separate detector regions (top, bottom, left, right, rear, front) and the sum of all detectors for the ^{60}Co source.

	top	**bottom**	**left**	**right**	**rear**	**front**	**sum**
meas response [$\frac{cps}{\gamma/s}$]	0.0179	0.0163	0.0350	0.0364	0.0358	0.0350	0.1768
sim response [$\frac{cps}{\gamma/s}$]	0.0236	0.0236	0.0460	0.0462	0.0464	0.0463	0.2170
MSR	0.76	0.69	0.76	0.79	0.77	0.76	0.81

Table 9: Ratios of the measured response of the RADOS RTM661/440*lnc* relative to the simulated response (MSR) for the separate detector regions (top, bottom, left, right, rear, front) and the sum of all detectors for the ^{137}Cs source.

	top	**bottom**	**left**	**right**	**rear**	**front**	**sum**
meas response [$\frac{cps}{\gamma/s}$]	0.0180	0.0168	0.0340	0.0400	0.0380	0.0373	0.1844
sim response [$\frac{cps}{\gamma/s}$]	0.0278	0.0277	0.0544	0.0538	0.0541	0.0544	0.2544
MSR	0.65	0.61	0.63	0.74	0.70	0.69	0.73

5.1.2 Changing the detector geometry

The RADOS device has dimensions as specified in table 1. According to the RADOS manual [4], the thickness of the six scintillation detectors is given as 5 cm, however, it is not stated whether this includes the 3 mm aluminum housing. In the previous simulation, the detectors were assumed to be 5 cm thick excluding the housing. To account for the possibility that the specified thickness includes the housing, the detector geometry is adjusted accordingly. A new simulation is conducted in the same manner as described in chapter 2, but using the adapted geometry. Figure 9 shows both the previously simulated response data from chapter 3 and the results from the adapted geometry. The response curve for the point source with the adapted detector geometry (silver) closely resembles that of the point source with the previous geometry (red) in shape, but shows lower response values overall. This can likely be attributed to the reduced detector size.

A comparison between the RADOS manufacturer's data and both the previous and newly obtained simulation results is made. The response data for the point source simulations with different geometries is very similar, with the adapted geometry showing a slightly lower response at low photon energies and a slightly higher response at high photon energies compared to the previous geometry. The simulation results for both the previous and the modified geometries exhibit comparable deviations from the manufacturer's data.

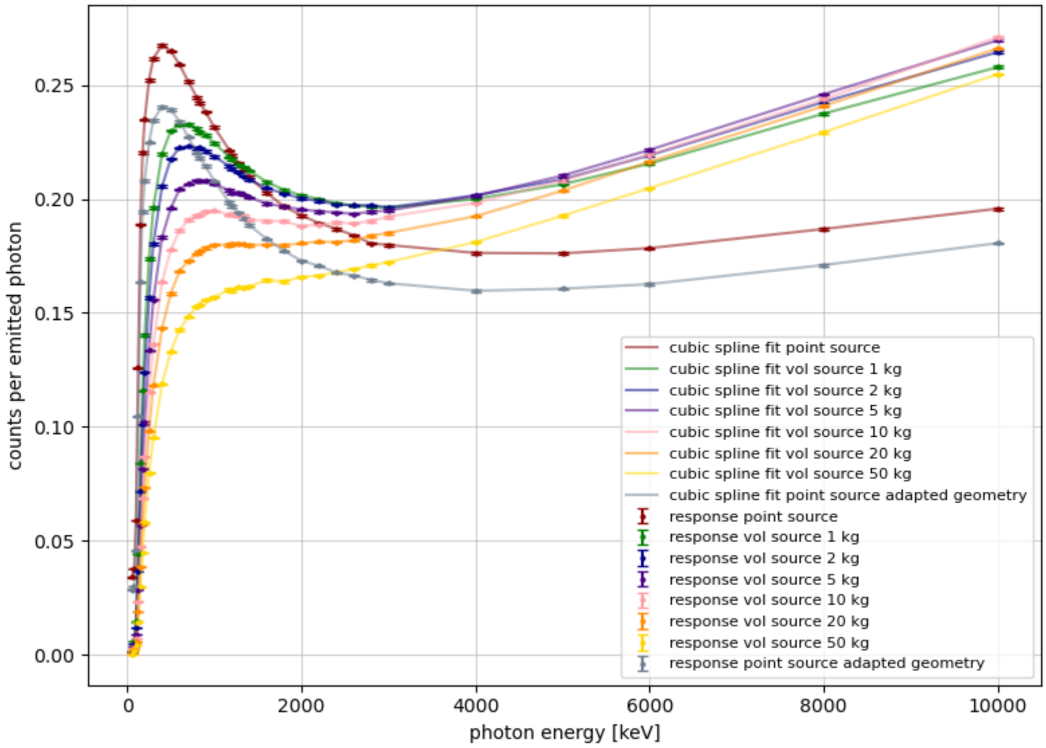

Figure 9: Simulated response curve of the RADOS device for isotropic sources emitting with an energy in the range of 50 keV to 10 MeV, including a simulation for an adapted detector geometry (silver).

To compare the simulated data, the measurement data for the ^{60}Co and ^{137}Cs sources placed in the center of the measurement chamber can be used, that can be seen in chapter 4. Table 10 provides a comparison between the measurement data with uncertainty considered to be below 1% and the simulated data with uncertainty in the order of 0.2%. Table 11 depicts the Measurement-to-Simulation ratio (MSR) as well as the average measured lnc factors, both of which with uncertainty considered to be below 1%.

Table 10: Comparison of the measured data to the simulated data for a point source and an adapted detector geometry.

	Measurement		**Simulation of adapted geometry**	
Nuclide	Response [cps]	Response per γ $[\frac{\text{cps}}{\gamma/s}]$	E_γ [keV]	Response per γ $[\frac{\text{cps}}{\gamma/s}]$
^{60}Co	6370	0.1768	1173, 1332	0.1949
^{137}Cs	5530	0.1844	662	0.2298

Table 11: Average measured lnc factors per photon and ratio of the measured response of the RADOS RTM661/440*lnc* relative to the simulated response (MSR) for a point source with adapted detector geometry.

Nuclide	**lnc per γ**	E_γ **[keV]**	**MSR**
^{60}Co	0.5	1173, 1332	0.91
^{137}Cs	0.501	662	0.80

For the case of ^{60}Co the MSR reaches a value of 91% compared to the old geometry with 81% (see table 7) and for the case of ^{137}Cs the MSR for the new geometry is 80% compared to the previous geometry with 0.73%. For both sources an increase in MSR by 10% (7% respectively) can be seen. The trend, that the simulated response resembles the measurement data more closely when reducing the size of the detector, is evident. However, it has to be noted, that the geometry of this simulation might not fully resemble the real RADOS device, since the detailed geometry is not known at this moment. In order to be able to conduct an accurate simulation, the details of the geometry would have to be clarified.

6 Conclusion

The RADOS RTM661/440*lnc* is a gamma counting measurement device used to determine the radiological classification of materials. To characterize its functionality, several FLUKA simulations were performed to determine the response to isotropic photon-emitting point and volume sources over a range of photon energies (see figure 6).

The simulated response data were compared to a response curve provided by the device's manufacturer as well as experimental measurements. A significant deviation was observed between the simulated response and the manufacturer's curve. To understand the cause of the deviation, the methodology used to derive the manufacturer's curve would need to be investigated. When comparing the simulated values to experimental measurements, the simulation results were found to be significantly higher than the measured values (see table 6). However the trend, that the simulated response resembles the measurement data more closely when reducing the size of the detectors is found (see table 10). To achieve more accurate simulations, detailed knowledge of the geometry of the physical device would be required.

Furthermore a simulation was conducted, modeling the six scintillation detectors of the device as individual detector regions. A comparison with measurement values showed that the simulated values consistently exceeded the measured values for all detectors (see tables 8 and 9). The magnitude of the deviation varies between the detectors as well as across different measurements. To characterize this deviation, further simulations and measurements would need to be conducted with different energies and different placements of the source.

Acknowledgments

Many thanks to Yann Pira and Frederic Aberle for providing their valuable advice on the measurements. Their insights were essential in ensuring the accuracy and reliability of the measured data.

References

[1] *Schweizer Strahlenschutzverordnung vom 22.6.2017 (StSV)*, February 2019.

[2] C. Theis. Clearance Limits for Radioactive Material at CERN. Technical Report EDMS 942170, CERN, March 2021.

[3] H. Vincke and C. Theis. Detector response of CERN-BGO low background device and its application for zoning. Technical Report EDMS 3018367, CERN, November 2024.

[4] Mirion Technologies (RADOS) GmbH. *Technical Handbook CheckPoint:Waste™ Premium*.

[5] Mirion Technologies. https://www.mirion.com/. Accessed [04.08.2025].

[6] N. Walter. *Development of an In-Situ Radiological Classification Technique for Material from CERN's Accelerator Facilities*. PhD thesis, Technische Universität München, November 2015.

[7] C. Ahdida, D. Bozzato, D. Calzolari, F. Cerutti, N. Charitonidis, A. Cimmino, A. Coronetti, G. L. D'Alessandro, A. Donadon Servelle, L. S. Esposito, R. Froeschl, R. García Alía, A. Gerbershagen, S. Gilardoni, D. Horváth, G. Hugo, A. Infantino, V. Kouskoura, A. Lechner, B. Lefebvre, G. Lerner, M. Magistris, A. Manousos, G. Moryc, F. Ogallar Ruiz, F. Pozzi, D. Prelipcean, S. Roesler, R. Rossi, M. Sabaté Gilarte, F. Salvat Pujol, P. Schoofs, V. Stránský, C. Theis, A. Tsinganis, R. Versaci, V. Vlachoudis, A. Waets, M. Widorski. *New Capabilities of the FLUKA Multi-Purpose Code*. *Frontiers in Physics 9*, page 788253, 2022.

[8] C. Theis, K.H. Buchegger, M. Brugger, D. Forkel-Wirth, S. Roesler, H.Vincke. *Interactive three dimensional visualization and creation of geometries for Monte Carlo calculations*. *Nuclear Instruments and Methods in Physics Research A 562*, pages 827–829, 2006.

[9] W. Demtröder. *Experimentalphysik 3. Atome, Moleküle und Festkörper*, volume 5. Springer, 2016.

[10] F. Aberle and R. Charousset. Instruction de travail. Contrôle du bon fonctionnement du RADOS RTM661/440Inc et du RADOS RTM644Inc. Technical Report EDMS 2213747, CERN, February 2020.

[11] F. Aberle. Instruction de travail. Mode opératoire pour l'utilisation du RADOS dans le cadre des mesures de libération. Technical Report EDMS 2149498, CERN, March 2020.

Appendices

A Raw response data of the simulations

Table 12: Response data obtained from the simulation for the point source (see subchapter 3.3), the point source with adapted detector geometry, such that the detectors are smaller (see section 5.1.2), and the 1 kg volume source (see subchapter 3.3), placed in the center of the measurement chamber.

	Point source		**Point source small det.**		**1 kg source**	
E_γ **[keV]**	response [$\frac{cps}{\gamma/s}$]	err [%]	response [$\frac{cps}{\gamma/s}$]	err [%]	response [$\frac{cps}{\gamma/s}$]	err [%]
50	3.412E-02	5.414E-01	2.860E-02	5.913E-01	1.415E-03	2.658E+00
80	3.775E-02	5.147E-01	3.020E-02	5.754E-01	5.994E-03	1.292E+00
100	5.903E-02	4.116E-01	4.600E-02	4.662E-01	1.467E-02	8.257E-01
125	1.260E-01	2.817E-01	1.048E-01	3.088E-01	4.436E-02	4.748E-01
150	1.888E-01	2.301E-01	1.637E-01	2.472E-01	8.413E-02	3.448E-01
175	2.203E-01	2.131E-01	1.943E-01	2.269E-01	1.160E-01	2.936E-01
200	2.348E-01	2.064E-01	2.081E-01	2.192E-01	1.402E-01	2.671E-01
250	2.523E-01	1.991E-01	2.248E-01	2.109E-01	1.738E-01	2.399E-01
300	2.617E-01	1.955E-01	2.346E-01	2.065E-01	1.963E-01	2.257E-01
400	2.674E-01	1.934E-01	2.405E-01	2.039E-01	2.199E-01	2.133E-01
500	2.648E-01	1.943E-01	2.393E-01	2.044E-01	2.300E-01	2.085E-01
600	2.589E-01	1.965E-01	2.339E-01	2.068E-01	2.324E-01	2.074E-01
700	2.515E-01	1.994E-01	2.271E-01	2.098E-01	2.328E-01	2.073E-01
800	2.445E-01	2.022E-01	2.201E-01	2.131E-01	2.308E-01	2.081E-01
834	2.423E-01	2.032E-01	2.181E-01	2.141E-01	2.290E-01	2.090E-01
900	2.382E-01	2.049E-01	2.143E-01	2.160E-01	2.279E-01	2.095E-01
1000	2.314E-01	2.079E-01	2.078E-01	2.194E-01	2.245E-01	2.111E-01
1173	2.213E-01	2.126E-01	1.984E-01	2.245E-01	2.183E-01	2.140E-01
1200	2.193E-01	2.135E-01	1.969E-01	2.253E-01	2.175E-01	2.144E-01
1274	2.159E-01	2.152E-01	1.941E-01	2.270E-01	2.153E-01	2.155E-01
1333	2.131E-01	2.166E-01	1.916E-01	2.285E-01	2.141E-01	2.161E-01
1400	2.097E-01	2.184E-01	1.885E-01	2.303E-01	2.124E-01	2.170E-01
1600	2.027E-01	2.221E-01	1.825E-01	2.341E-01	2.075E-01	2.195E-01
1800	1.967E-01	2.255E-01	1.772E-01	2.375E-01	2.040E-01	2.214E-01
2000	1.928E-01	2.278E-01	1.729E-01	2.405E-01	2.015E-01	2.228E-01
2200	1.894E-01	2.298E-01	1.707E-01	2.421E-01	2.000E-01	2.236E-01
2400	1.869E-01	2.313E-01	1.677E-01	2.442E-01	1.980E-01	2.248E-01
2600	1.840E-01	2.332E-01	1.664E-01	2.451E-01	1.971E-01	2.252E-01
2800	1.805E-01	2.354E-01	1.645E-01	2.466E-01	1.967E-01	2.255E-01
3000	1.798E-01	2.358E-01	1.630E-01	2.477E-01	1.961E-01	2.258E-01
4000	1.763E-01	2.382E-01	1.597E-01	2.502E-01	2.000E-01	2.236E-01
5000	1.761E-01	2.383E-01	1.606E-01	2.495E-01	2.064E-01	2.201E-01
6000	1.784E-01	2.367E-01	1.626E-01	2.480E-01	2.155E-01	2.154E-01
8000	1.868E-01	2.314E-01	1.710E-01	2.418E-01	2.374E-01	2.052E-01
10000	1.957E-01	2.261E-01	1.806E-01	2.353E-01	2.578E-01	1.970E-01

Table 13: Response data obtained from the simulation for the 2, 5 and 10 kg volume sources placed in the center of the measurement chamber (see subchapter 3.3).

	2 kg source		**5 kg source**		**10 kg source**	
E_γ [keV]	response [$\frac{cps}{\gamma/s}$]	err [%]	response [$\frac{cps}{\gamma/s}$]	err [%]	response [$\frac{cps}{\gamma/s}$]	err [%]
50	1.143E-03	2.958E+00	8.170E-04	3.499E+00	6.640E-04	3.881E+00
80	4.845E-03	1.437E+00	3.649E-03	1.655E+00	3.001E-03	1.825E+00
100	1.208E-02	9.098E-01	9.029E-03	1.052E+00	7.443E-03	1.159E+00
125	3.673E-02	5.218E-01	2.872E-02	5.901E-01	2.339E-02	6.539E-01
150	7.183E-02	3.731E-01	5.694E-02	4.191E-01	4.738E-02	4.594E-01
175	1.012E-01	3.143E-01	8.170E-02	3.499E-01	6.886E-02	3.811E-01
200	1.239E-01	2.841E-01	1.020E-01	3.132E-01	8.700E-02	3.390E-01
250	1.567E-01	2.526E-01	1.336E-01	2.736E-01	1.155E-01	2.942E-01
300	1.804E-01	2.354E-01	1.557E-01	2.534E-01	1.364E-01	2.708E-01
400	2.056E-01	2.205E-01	1.833E-01	2.335E-01	1.637E-01	2.472E-01
500	2.176E-01	2.144E-01	1.960E-01	2.259E-01	1.777E-01	2.373E-01
600	2.224E-01	2.121E-01	2.042E-01	2.213E-01	1.861E-01	2.318E-01
700	2.230E-01	2.118E-01	2.066E-01	2.200E-01	1.908E-01	2.289E-01
800	2.221E-01	2.122E-01	2.082E-01	2.192E-01	1.928E-01	2.278E-01
834	2.225E-01	2.120E-01	2.077E-01	2.194E-01	1.930E-01	2.276E-01
900	2.208E-01	2.128E-01	2.080E-01	2.192E-01	1.946E-01	2.267E-01
1000	2.186E-01	2.139E-01	2.065E-01	2.201E-01	1.948E-01	2.266E-01
1173	2.143E-01	2.160E-01	2.037E-01	2.216E-01	1.931E-01	2.275E-01
1200	2.133E-01	2.165E-01	2.028E-01	2.220E-01	1.933E-01	2.275E-01
1274	2.117E-01	2.173E-01	2.026E-01	2.222E-01	1.924E-01	2.280E-01
1333	2.099E-01	2.183E-01	2.018E-01	2.226E-01	1.927E-01	2.278E-01
1400	2.084E-01	2.190E-01	2.007E-01	2.232E-01	1.909E-01	2.289E-01
1600	2.048E-01	2.210E-01	1.980E-01	2.247E-01	1.903E-01	2.292E-01
1800	2.023E-01	2.224E-01	1.966E-01	2.255E-01	1.902E-01	2.293E-01
2000	2.002E-01	2.235E-01	1.954E-01	2.262E-01	1.881E-01	2.306E-01
2200	1.991E-01	2.241E-01	1.945E-01	2.267E-01	1.887E-01	2.302E-01
2400	1.976E-01	2.250E-01	1.941E-01	2.270E-01	1.896E-01	2.297E-01
2600	1.972E-01	2.252E-01	1.934E-01	2.274E-01	1.893E-01	2.298E-01
2800	1.972E-01	2.252E-01	1.944E-01	2.268E-01	1.903E-01	2.292E-01
3000	1.962E-01	2.258E-01	1.949E-01	2.265E-01	1.922E-01	2.281E-01
4000	2.016E-01	2.227E-01	2.013E-01	2.229E-01	1.982E-01	2.246E-01
5000	2.086E-01	2.190E-01	2.102E-01	2.181E-01	2.081E-01	2.192E-01
6000	2.191E-01	2.136E-01	2.215E-01	2.125E-01	2.194E-01	2.135E-01
8000	2.425E-01	2.031E-01	2.459E-01	2.017E-01	2.437E-01	2.026E-01
10000	2.644E-01	1.945E-01	2.696E-01	1.926E-01	2.710E-01	1.921E-01

Table 14: Response data obtained from the simulation for the 20 and 50 volume sources placed in the center of the measurement chamber and the 50 kg volume sourced placed at the bottom of the measurement chamber in the middle of the bottom detector (see subchapter 3.3).

	20 kg source		**50 kg source**		**50 kg source bottom**	
E_γ [keV]	response [$\frac{cps}{\gamma/s}$]	err [%]	response [$\frac{cps}{\gamma/s}$]	err [%]	response [$\frac{cps}{\gamma/s}$]	err [%]
50	5.530E-04	4.252E+00	3.790E-04	5.137E+00	2.380E-04	6.482E+00
80	2.342E-03	2.066E+00	1.803E-03	2.355E+00	1.375E-03	2.697E+00
100	5.811E-03	1.312E+00	4.371E-03	1.513E+00	3.788E-03	1.625E+00
125	1.916E-02	7.225E-01	1.459E-02	8.279E-01	1.310E-02	8.736E-01
150	3.864E-02	5.087E-01	3.000E-02	5.773E-01	2.848E-02	5.926E-01
175	5.739E-02	4.174E-01	4.496E-02	4.716E-01	4.517E-02	4.705E-01
200	7.320E-02	3.696E-01	5.829E-02	4.142E-01	5.884E-02	4.122E-01
250	9.840E-02	3.188E-01	7.972E-02	3.542E-01	8.245E-02	3.483E-01
300	1.182E-01	2.909E-01	9.533E-02	3.239E-01	1.011E-01	3.145E-01
400	1.435E-01	2.640E-01	1.190E-01	2.898E-01	1.268E-01	2.809E-01
500	1.586E-01	2.511E-01	1.330E-01	2.742E-01	1.427E-01	2.648E-01
600	1.684E-01	2.437E-01	1.426E-01	2.648E-01	1.536E-01	2.551E-01
700	1.729E-01	2.405E-01	1.483E-01	2.596E-01	1.606E-01	2.495E-01
800	1.760E-01	2.384E-01	1.529E-01	2.557E-01	1.661E-01	2.454E-01
834	1.772E-01	2.376E-01	1.536E-01	2.551E-01	1.670E-01	2.447E-01
900	1.785E-01	2.367E-01	1.557E-01	2.535E-01	1.703E-01	2.423E-01
1000	1.799E-01	2.358E-01	1.569E-01	2.525E-01	1.724E-01	2.408E-01
1173	1.798E-01	2.359E-01	1.603E-01	2.498E-01	1.750E-01	2.390E-01
1200	1.803E-01	2.355E-01	1.596E-01	2.503E-01	1.765E-01	2.380E-01
1274	1.805E-01	2.354E-01	1.613E-01	2.490E-01	1.775E-01	2.374E-01
1333	1.801E-01	2.356E-01	1.611E-01	2.491E-01	1.771E-01	2.377E-01
1400	1.797E-01	2.359E-01	1.617E-01	2.487E-01	1.779E-01	2.371E-01
1600	1.800E-01	2.357E-01	1.643E-01	2.467E-01	1.798E-01	2.359E-01
1800	1.796E-01	2.359E-01	1.638E-01	2.471E-01	1.821E-01	2.343E-01
2000	1.806E-01	2.353E-01	1.658E-01	2.456E-01	1.834E-01	2.335E-01
2200	1.812E-01	2.349E-01	1.664E-01	2.451E-01	1.850E-01	2.325E-01
2400	1.811E-01	2.350E-01	1.678E-01	2.441E-01	1.863E-01	2.317E-01
2600	1.819E-01	2.345E-01	1.693E-01	2.430E-01	1.886E-01	2.302E-01
2800	1.838E-01	2.333E-01	1.708E-01	2.419E-01	1.894E-01	2.297E-01
3000	1.851E-01	2.324E-01	1.723E-01	2.409E-01	1.917E-01	2.284E-01
4000	1.924E-01	2.280E-01	1.811E-01	2.350E-01	2.013E-01	2.229E-01
5000	2.036E-01	2.216E-01	1.926E-01	2.279E-01	2.127E-01	2.168E-01
6000	2.163E-01	2.150E-01	2.047E-01	2.210E-01	2.246E-01	2.110E-01
8000	2.407E-01	2.038E-01	2.293E-01	2.088E-01	2.501E-01	1.999E-01
10000	2.660E-01	1.939E-01	2.547E-01	1.982E-01	2.762E-01	1.903E-01

Table 15: Response data obtained from the simulation for a point source and separate detector regions, namely the top, bottom and left detector (see section 5.1.1).

	top detector		**bottom detector**		**left detector**	
E_γ [keV]	response [$\frac{cps}{\gamma/s}$]	err [%]	response [$\frac{cps}{\gamma/s}$]	err [%]	response [$\frac{cps}{\gamma/s}$]	err [%]
50	3.185E-03	1.772E+00	3.162E-03	1.778E+00	6.219E-03	1.268E+00
80	3.473E-03	1.697E+00	3.524E-03	1.685E+00	6.879E-03	1.206E+00
100	4.574E-03	1.479E+00	4.616E-03	1.472E+00	9.151E-03	1.045E+00
125	9.685E-03	1.016E+00	9.401E-03	1.031E+00	1.969E-02	7.126E-01
150	1.746E-02	7.567E-01	1.752E-02	7.555E-01	3.467E-02	5.370E-01
175	2.228E-02	6.700E-01	2.269E-02	6.639E-01	4.435E-02	4.748E-01
200	2.414E-02	6.437E-01	2.420E-02	6.428E-01	4.820E-02	4.555E-01
250	2.664E-02	6.127E-01	2.650E-02	6.143E-01	5.259E-02	4.361E-01
300	2.808E-02	5.967E-01	2.826E-02	5.948E-01	5.509E-02	4.261E-01
400	2.922E-02	5.850E-01	2.908E-02	5.865E-01	5.705E-02	4.187E-01
500	2.907E-02	5.865E-01	2.876E-02	5.897E-01	5.614E-02	4.221E-01
600	2.823E-02	5.951E-01	2.827E-02	5.948E-01	5.528E-02	4.253E-01
700	2.758E-02	6.021E-01	2.733E-02	6.049E-01	5.371E-02	4.315E-01
800	2.657E-02	6.135E-01	2.665E-02	6.126E-01	5.212E-02	4.380E-01
834	2.614E-02	6.185E-01	2.640E-02	6.154E-01	5.182E-02	4.393E-01
900	2.595E-02	6.207E-01	2.610E-02	6.189E-01	5.058E-02	4.446E-01
1000	2.522E-02	6.297E-01	2.527E-02	6.290E-01	4.947E-02	4.496E-01
1173	2.403E-02	6.450E-01	2.410E-02	6.441E-01	4.679E-02	4.623E-01
1200	2.402E-02	6.452E-01	2.389E-02	6.470E-01	4.684E-02	4.621E-01
1274	2.348E-02	6.527E-01	2.327E-02	6.555E-01	4.618E-02	4.653E-01
1333	2.313E-02	6.576E-01	2.320E-02	6.566E-01	4.532E-02	4.698E-01
1400	2.279E-02	6.624E-01	2.274E-02	6.632E-01	4.474E-02	4.728E-01
1600	2.183E-02	6.768E-01	2.252E-02	6.664E-01	4.294E-02	4.826E-01
1800	2.152E-02	6.816E-01	2.153E-02	6.816E-01	4.164E-02	4.901E-01
2000	2.110E-02	6.883E-01	2.093E-02	6.913E-01	4.105E-02	4.936E-01
2200	2.064E-02	6.961E-01	2.060E-02	6.967E-01	4.051E-02	4.968E-01
2400	2.057E-02	6.972E-01	2.052E-02	6.981E-01	3.973E-02	5.017E-01
2600	2.002E-02	7.068E-01	2.015E-02	7.045E-01	3.929E-02	5.045E-01
2800	1.997E-02	7.077E-01	1.976E-02	7.114E-01	3.881E-02	5.076E-01
3000	1.988E-02	7.092E-01	1.985E-02	7.097E-01	3.871E-02	5.083E-01
4000	1.972E-02	7.121E-01	1.992E-02	7.085E-01	3.785E-02	5.140E-01
5000	1.994E-02	7.082E-01	1.992E-02	7.085E-01	3.841E-02	5.102E-01
6000	2.054E-02	6.978E-01	2.079E-02	6.936E-01	3.833E-02	5.108E-01
8000	2.225E-02	6.704E-01	2.211E-02	6.726E-01	4.121E-02	4.926E-01
10000	2.383E-02	6.478E-01	2.353E-02	6.519E-01	4.352E-02	4.793E-01

Table 16: Response data obtained from the simulation for a point source and separate detector regions, namely the right, rear and front detector (see section 5.1.1).

	right detector		**rear detector**		**front detector**	
E_γ [keV]	response [$\frac{cps}{\gamma/s}$]	err [%]	response [$\frac{cps}{\gamma/s}$]	err [%]	response [$\frac{cps}{\gamma/s}$]	err [%]
50	6.260E-03	1.264E+00	6.366E-03	1.253E+00	6.230E-03	1.267E+00
80	6.937E-03	1.201E+00	6.774E-03	1.215E+00	6.849E-03	1.208E+00
100	9.194E-03	1.043E+00	9.158E-03	1.045E+00	9.099E-03	1.048E+00
125	1.958E-02	7.147E-01	1.970E-02	7.124E-01	1.960E-02	7.144E-01
150	3.512E-02	5.336E-01	3.511E-02	5.337E-01	3.512E-02	5.336E-01
175	4.479E-02	4.725E-01	4.397E-02	4.769E-01	4.438E-02	4.747E-01
200	4.856E-02	4.538E-01	4.786E-02	4.571E-01	4.835E-02	4.548E-01
250	5.269E-02	4.357E-01	5.292E-02	4.347E-01	5.227E-02	4.374E-01
300	5.501E-02	4.264E-01	5.489E-02	4.268E-01	5.513E-02	4.259E-01
400	5.656E-02	4.205E-01	5.659E-02	4.203E-01	5.701E-02	4.188E-01
500	5.650E-02	4.207E-01	5.620E-02	4.218E-01	5.673E-02	4.198E-01
600	5.492E-02	4.267E-01	5.521E-02	4.256E-01	5.521E-02	4.256E-01
700	5.322E-02	4.335E-01	5.339E-02	4.328E-01	5.393E-02	4.306E-01
800	5.218E-02	4.378E-01	5.204E-02	4.383E-01	5.227E-02	4.374E-01
834	5.190E-02	4.389E-01	5.185E-02	4.392E-01	5.131E-02	4.415E-01
900	5.081E-02	4.437E-01	5.053E-02	4.449E-01	5.078E-02	4.437E-01
1000	4.891E-02	4.522E-01	4.922E-02	4.507E-01	4.931E-02	4.503E-01
1173	4.738E-02	4.594E-01	4.736E-02	4.595E-01	4.712E-02	4.607E-01
1200	4.692E-02	4.616E-01	4.620E-02	4.652E-01	4.670E-02	4.627E-01
1274	4.618E-02	4.653E-01	4.558E-02	4.684E-01	4.582E-02	4.672E-01
1333	4.509E-02	4.709E-01	4.548E-02	4.689E-01	4.564E-02	4.681E-01
1400	4.484E-02	4.723E-01	4.424E-02	4.754E-01	4.479E-02	4.725E-01
1600	4.308E-02	4.818E-01	4.315E-02	4.814E-01	4.289E-02	4.829E-01
1800	4.185E-02	4.888E-01	4.170E-02	4.897E-01	4.210E-02	4.874E-01
2000	4.076E-02	4.953E-01	4.113E-02	4.931E-01	4.117E-02	4.928E-01
2200	4.028E-02	4.982E-01	4.046E-02	4.971E-01	4.045E-02	4.972E-01
2400	3.955E-02	5.029E-01	4.018E-02	4.989E-01	3.985E-02	5.010E-01
2600	3.926E-02	5.047E-01	3.943E-02	5.036E-01	3.911E-02	5.057E-01
2800	3.860E-02	5.090E-01	3.836E-02	5.106E-01	3.841E-02	5.102E-01
3000	3.833E-02	5.108E-01	3.806E-02	5.126E-01	3.846E-02	5.099E-01
4000	3.784E-02	5.141E-01	3.775E-02	5.147E-01	3.770E-02	5.150E-01
5000	3.793E-02	5.134E-01	3.796E-02	5.133E-01	3.813E-02	5.121E-01
6000	3.893E-02	5.069E-01	3.885E-02	5.074E-01	3.867E-02	5.085E-01
8000	4.096E-02	4.941E-01	4.079E-02	4.951E-01	4.124E-02	4.925E-01
10000	4.331E-02	4.805E-01	4.347E-02	4.797E-01	4.352E-02	4.794E-01